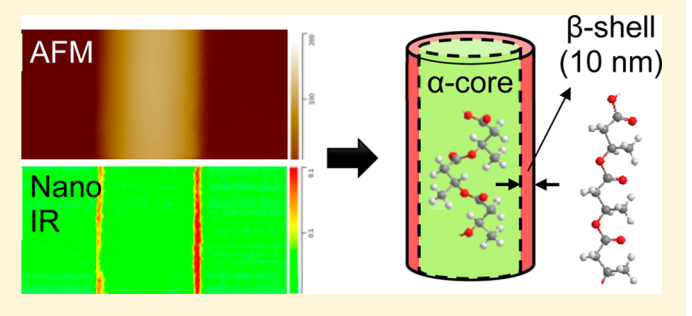
# **Macromolecules**

# Polymorphic Distribution in Individual Electrospun Poly[(R)-3hydroxybutyrate-co-(R)-3-hydroxyhexanoate] (PHBHx) Nanofibers

Liang Gong,<sup>†</sup> D. Bruce Chase,<sup>†</sup> Isao Noda,<sup>†,‡</sup> Curtis A. Marcott,<sup>†,§</sup> Jinglin Liu,<sup>†</sup> David C. Martin,<sup>†</sup> Chaoying Ni,<sup>†</sup> and John F. Rabolt\*,<sup>†</sup>

ABSTRACT: We have observed, for the first time, a heterogeneous spatial distribution of crystalline polymorphs in a single electrospun polymer nanofiber. Two crystalline polymorphs of PHBHx, the thermodynamically stable  $\alpha$ -form consisting of chains with a 21 helical conformation and the metastable  $\beta$ -form consisting of chains with a planar zigzag conformation, are spatially distributed as a core-shell structure composed of an  $\alpha$ -form-rich core and a  $\beta$ -form-rich shell. In addition, it was found that the thickness of the shell is independent of the fiber diameter. The characterization of crystalline polymorphic distribution in individual nanofibers



has been made possible by utilizing a technique combining atomic force microscopy (AFM) and infrared spectroscopy (IR), which simultaneously provides the nanoscale spatial resolution and crystalline phase specificity. Based on the experimental results, a possible generation mechanism of this polymorphic heterogeneous core-shell structure is proposed. The implications of this core-shell model on fiber properties are also discussed.

# INTRODUCTION

Electrospinning, a technique which relies on self-organization via electric charges and their interaction with an applied field, is an efficient and versatile technique to produce ultrafine fibers with diameters down to the range of a few tens of nanometers. Electrospun nanofibers find interesting applications in areas including tissue engineering,<sup>2</sup> drug delivery,<sup>3</sup> sensors and actuators,<sup>4</sup> energy storage, food processing,<sup>5</sup> and water filtration,6 leading to a growing industrial demand for such fibers. Because of the strong stretching forces and fast solvent evaporation kinetics associated with the electrospinning process, the electrospun fibers can have a distinct crystallization behavior compared to the bulk materials. This can lead to the formation of metastable phases or crystalline polymorphs.<sup>7–13</sup> For some polymeric materials, more than one crystalline polymorph can be found in the electrospun nanofibers, and the population of each polymorph can often be controlled by varying the electrospinning conditions. For example, our previous study<sup>14</sup> demonstrated the coexistence of two crystalline polymorphs in the electrospun nanofibers of biobased poly[(R)-3-hydroxybutyrate-co-(R)-3-hydroxyhexanoate](PHBHx) collected with modified collectors. In addition, the concentration of the two crystalline polymorphs, the thermodynamically stable  $\alpha$ -form with chains exhibiting a  $2_1$ helical conformation and the strain-induced metastable  $\beta$ -form with chains adopting a planar zigzag conformation, can be affected by the collection methods. Y4 The implications of these observations are far-reaching since the crystalline structure of a

polymer plays an important role in its properties which are manifested after processing. In order to further elucidate the crystallization behavior of the polymer chains during the electrospinning process, studies on the internal structure of a single electrospun nanofiber, including the spatial distribution of the crystalline polymorphs, become essential. Unfortunately, very few techniques can simultaneously provide the necessary spatial resolution and phase sensitivity/specificity.

The combination of atomic force microscopy (AFM) and infrared (IR) spectroscopy can overcome these technical limitations. This new technique, known as AFM-IR, is based on the photothermal induced resonance effect (PTIR). 15-20 It is a powerful tool which provides topographic information that can be correlated with chemical, conformational, and molecular orientation information at a spatial resolution of 50-100 nm. Unlike conventional FT-IR spectroscopy, the AFM-IR technique uses a sharp, gold-coated AFM tip to detect the rapid thermal expansion of the sample caused by the absorption of short (10 ns) pulses of IR radiation. When the monochromatic laser radiation approaches an IR frequency that excites a molecular vibration in the sample, the light is absorbed and induces a rapid thermal expansion of the sample, which is in contact with the AFM tip. This results in a simultaneous deflection of the AFM tip and causes a "ring down" of the cantilever at its natural deflection resonant

Received: May 24, 2017 Published: July 11, 2017

Department of Materials Science and Engineering, University of Delaware, Newark, Delaware 19716, United States

<sup>&</sup>lt;sup>‡</sup>Danimer Scientific, Bainbridge, Georgia 39818, United States

<sup>§</sup>Light Light Solutions, Athens, Georgia 30608, United States

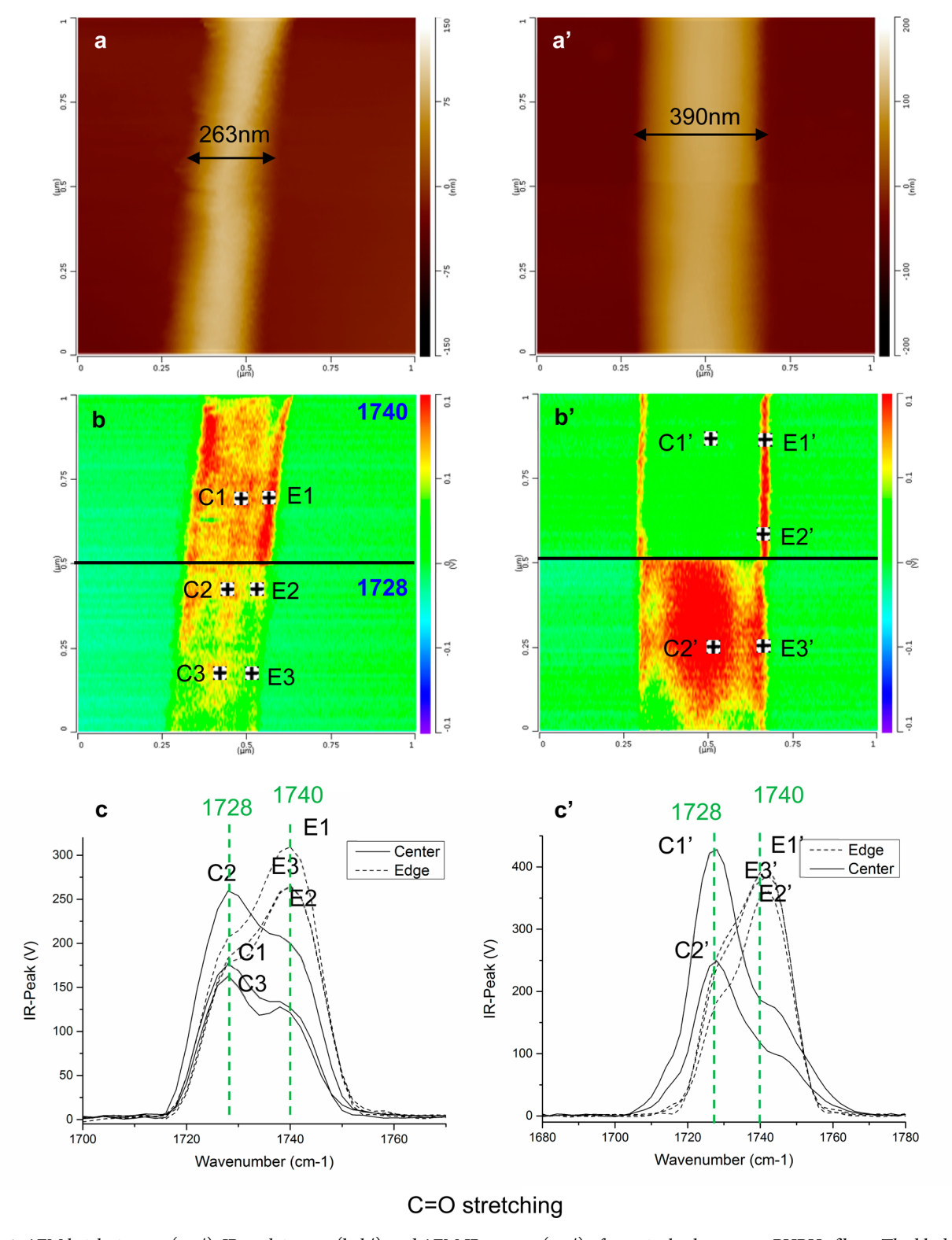


Figure 1. AFM height images (a, a'), IR peak images (b, b'), and AFM-IR spectra (c, c') of two single electrospun PHBHx fibers. The black spots in (b) and (b') indicate the position of the AFM tip when collecting the AFM-IR spectra.

frequencies as the heat dissipates. These motions of the cantilever are "detected" by a second laser beam reflected off the top of the cantilever, and this signal is measured using a position-sensitive photodetector. The resonance amplitude induced in the cantilever is proportional to the amount of IR radiation absorbed by the sample. Thus, the resulting AFM-IR spectrum is obtained by measuring the ring-down

amplitudes while tuning the IR laser over the IR fingerprint region. More details concerning this AFM-IR instrument can be found elsewhere. The development of the AFM-IR technique, with the fine spatial resolution provided by the AFM tip and the phase sensitivity provided by the IR spectroscopy, allows us, for the first time, to probe the spatial

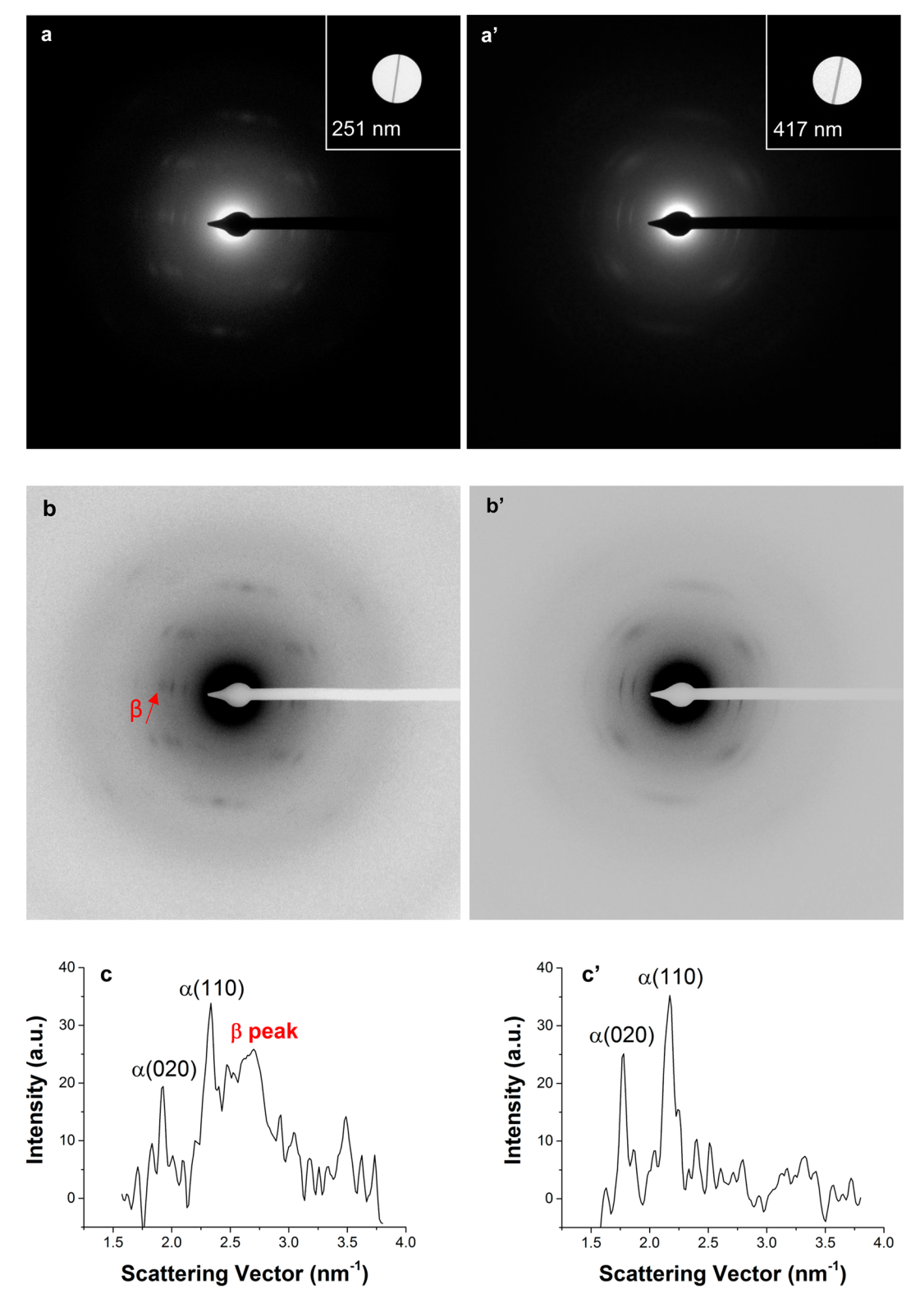


Figure 2. Original (a, a') and contrast-inverted (b, b') SAED patterns of two individual electrospun PHBHx nanofibers with diameters of 251 and 417 nm, respectively. The insets are bright-field TEM images of the two fibers. The intensity profiles of (a) and (a') along the equatorial line are plotted in (c) and (c'), respectively.

distribution of crystalline polymorphs in a single electrospun nanofiber.

In this study we report the first investigation of polymorphic distribution in single electrospun nanofibers utilizing the AFM-IR technique. Bio-based PHBHx nanofibers were fabricated by

electrospinning onto the tapered edge of a high-speed rotary disk. The coexistence of the  $\alpha$ - and  $\beta$ -form crystalline polymorphs in single nanofibers was confirmed by both AFM-IR and selected area electron diffraction (SAED) via low dose TEM. In addition, the dependence of the  $\beta$ -content

and the molecular orientation on fiber size were investigated by these two techniques at the single fiber scale. Furthermore, the spatial distribution of the two polymorphs throughout individual fibers with different diameters was examined by AFM-IR spectroscopy and imaging at a spatial resolution of 50 nm.

#### EXPERIMENTAL SECTION

**Polymer.** The bacterially produced poly(3-hydroxybutyrate-co-3-hydroxyhexanoate) (PHBHx) with 3.9 mol % hydroxyhexanoate (Hx) comonomer content ( $M_{\rm w}=843\,000$  g/mol, PDI = 2.2) was supplied by the Procter & Gamble Company. The polymer was purified by dissolving in chloroform (Fisher Scientific) followed by filtration and subsequent precipitation in hexane (Fisher Scientific). The solvent for electrospinning, 1,1,1,3,3,3-hexafluoro-2-propanol (HFIP), was purchased from Sigma-Aldrich and used as received.

Electrospinning. A 1 wt % electrospinning solution was prepared by dissolving the purified PHBHx in HFIP and stirring at 60 °C overnight to ensure complete dissolution. At room temperature, the polymer solution was loaded into a 3 mL BD plastic syringe with a 21 gauge stainless steel needle, which was connected to the positive terminal of a high-voltage supply held at 10 kV. A 5 mm thick, negatively charged (-5 kV) rotary disk was used to collect macroscopically aligned electrospun nanofibers. The angular velocity of the rotary disk was set to 3500 rpm, corresponding to a linear velocity of 1117 m/min at the flat edge. The working distance and solution pumping rate were 25 cm and 0.5 mL/h, respectively. Mid-IR (900-3600 cm<sup>-1</sup>) transparent silicon wafers (Addison Engineering, Inc.) were cut into 5 mm (width) × 8 mm (length) pieces and stuck to the edge of the rotary disk. During electrospinning, the fibers were electrospun directly onto the silicon wafer to maintain a good contact between the fiber and the substrate. The density of fibers on the silicon wafer can be easily adjusted by controlling the length of electrospinning time, which, for this study, was set to 45 s to obtain an approximate fiber density of 2 fibers/mm (length). After fiber deposition, the silicon wafers were put in vacuum for 24 h to remove any residual solvent prior to further investigation.

**Microtoming.** A bundle of rotary disk aligned nanofibers were parallel embedded in 2 Ton epoxy (ITW Devcon) prior to microtoming. After curing, 250 nm thick sections were cut by microtoming (Leica Ultracut UCT) at room temperature. The thin sections were later transferred to a 10 mm × 10 mm ZnS flat for AFM-IR studies.

Selected Area Electron Diffraction (SAED). SAED patterns and bright-field images were recorded by transmission electron microscopy (TEM, Tecnai G2 12) with a low-dose CCD camera using an accelerating voltage of 120 kV. The nanofibers were deposited on 400 mesh copper grids coated with carbon to reduce specimen damage. The diffraction patterns were obtained at a fixed camera length of 2.1 m. A thin layer of gold polycrystals was sputtered on each of the copper grid before the deposition of the fibers, which was used to calibrate the camera constant and correct any system distortion.

AFM-IR Measurement: Spectroscopy vs Imaging. Our nanoscale infrared measurements were carried out with a nanoIR2 platform (Anasys Instruments, Santa Barbara, CA), which focuses radiation from a tunable IR laser source onto a location on the sample top surface from above. Secondary Agold-coated SiN AFM tip (Anasys Instruments) with a nominal tip radius of 20 nm was used to examine the fibers in contact mode. The power of the incident IR laser was adjusted to approximately 2% of the open beam intensity for this study in order to obtain a good ring-down signal. Also, an additional mesh filter was placed in front of the IR laser to further attenuate the beam in order to avoid sample melting/softening. For IR mapping, the system was tuned to coordinate the update of the IR signal and the pixel rate of the image. The AFM height and IR peak image were first-order flattened using the instrument's built-in software (Analysis Studio, Anasys Instruments). The AFM-IR spectra were collected with a data point spacing of 2 cm<sup>-1</sup>, coaveraging 256 cantilever ring-downs within the spectral range 1680–1780 cm<sup>-1</sup>. The actual spectral

resolution in this wavenumber range is 4 cm<sup>-1</sup>, which is the laser line width. For each sampling spot on the fibers, five spectra from the same position were averaged to reach a satisfactory signal-to-noise ratio. All measurements were carried out under ambient conditions.

#### ■ RESULTS AND DISCUSSION

Macroscopically aligned, electrospun PHBHx nanofibers can be obtained by using a rotary disk as the fiber collector. <sup>14</sup> In this study, individual PHBHx nanofibers from the same batch were examined by AFM-IR. Figures 1a and 1a' display the AFM height images of two, single, rotary disk aligned fibers. The two fibers differ in size with diameters of 263 and 390 nm, respectively. Our previous study<sup>14</sup> showed that the straininduced, metastable  $\beta$ -form crystalline structure, with extended polymer chains adopting a planar zigzag conformation, was introduced when the fibers were collected on a high-speed rotary disk. Current results suggest that under this specific electrospinning condition the appearance of the  $\beta$ -crystalline phase is indicated by the characteristic IR absorption peak at 1740 cm<sup>-1</sup> in the IR spectrum. The IR absorption peak at 1728 cm<sup>-1</sup> is characteristic of the  $\alpha$ -crystalline phase, which is the thermodynamically stable crystal structure of PHBHx. 14 In order to investigate the spatial distribution of the two crystalline phases in the nanofibers, we imaged the two single fibers by tuning the frequency of the incident IR laser to 1740 and 1728 cm<sup>-1</sup>, the two characteristic frequencies corresponding to the  $\beta$ form and  $\alpha$ -form crystalline structure, respectively. The IR images are shown in Figures 1b and 1b'. For each IR image, the upper half was recorded at 1740 cm<sup>-1</sup> and the lower half at 1728 cm<sup>-1</sup>. By carefully examining these IR images, we can make several observations. First, when comparing Figures 1b and 1b', it is observed that both fibers have detectable IR absorption at 1740 and 1728 cm<sup>-1</sup>, indicating the coexistence of the  $\alpha$ - and  $\beta$ -crystalline phase at the single fiber scale. In addition, under the same mapping conditions, the thinner fiber (263 nm) has higher absorption at 1740 cm<sup>-1</sup> yet lower absorption at 1728 cm<sup>-1</sup>, indicating that the thinner fiber tends to have higher  $\beta$ -content than the thicker fiber (390 nm). Because the two fibers were fabricated under the same electrospinning conditions, the difference in diameter should be due to the different stretching forces they experienced during electrospinning and collection. Assuming extensional strain, the draw ratio of the 263 nm fiber is approximately 2.2 times larger than that of the 390 nm fiber. Since a higher draw ratio favors an extended chain, more molecular chains in the thinner fiber would be found in the planar zigzag conformation and pack to form the  $\beta$ -crystalline form.

The coexistence of both  $\alpha$ - and  $\beta$ -form crystal structures in single PHBHx nanofibers as well as the dependence of the  $\beta$ form content on fiber diameter is reaffirmed by the SAED patterns of individual PHBHx nanofibers. Figures 2a and 2a' display the original SAED patterns of two single PHBHx nanofibers from the same batch. The insets show the brightfield TEM images of the two single fibers. The diameters of the two fibers are 251 and 417 nm, respectively, which are comparable with those of the two fibers in the AFM-IR study. For comparative purposes, the original SAED patterns were contrast-inverted as shown in Figures 2b and 2b'. By comparing the two inverted SAED patterns, it is observed that the equatorial arcs assigned to the  $\beta$ -form crystal plane 14 are clearly visible in Figure 2b (indicated by the red arrow), while in Figure 2b' they can barely be recognized. For each of the SAED patterns, the intensity profile along the equatorial line was

plotted in Figures 2c and 2c' correspondingly against the scattering vector (1/d, reciprocal of space distance). Obviously, the intensity of the  $\beta$ -peak in Figure 2c is much higher than that in Figures 2c', indicating that the thinner fiber contains more  $\beta$ form crystals than the thicker fiber. In addition, it is also observed that the arcs in Figures 2b are less tangentially spread, or have a smaller central angle than those in Figures 2b', which indicates that the thinner fiber (251 nm) has a higher molecular orientation compared to the thicker fiber (417 nm). That is both the content of the  $\beta$ -form crystalline structure and the degree of molecular orientation in a single electrospun PHBHx nanofiber increase as the fiber diameter decreases. On the basis of the results from the AFM-IR and SAED studies, we observed a strong correlation between the  $\beta$ -form content in single PHBHx fibers and the fiber diameter, which is governed by the stretching forces experienced during the electrospinning and nanofiber collection process. The thinner the fibers are, the higher the  $\beta$ -form content and the higher the degree of molecular orientation.

The second observation we made from the IR images in Figures 1b and 1b' is that for both of the fibers the absorption at 1740 cm<sup>-1</sup> is always higher along the fiber edges, especially in Figure 1b' where the absorption is almost completely concentrated on the two edges. This observation suggests a heterogeneous spatial distribution of the  $\alpha$ - and  $\beta$ -crystalline structures throughout the fiber. More importantly, it suggests an interesting core—shell structure where the shell contains much more  $\beta$ -crystalline polymorph than the core. In addition, by carefully examining the two IR images, we found that the thickness of the shell, which is indicated by the width of the red lines along the fiber edges, is approximately 10 nm regardless of the fiber size.

In order to test our hypothesis of a core-shell structure for the fiber, for each of the two fibers AFM-IR spectra were collected at different positions where the IR image indicates the existence of heterogeneity. The AFM-IR spectra are shown in Figures 1c and 1c'. All the AFM-IR spectra have two characteristic peaks at 1740 and 1728 cm<sup>-1</sup>, which are known<sup>14</sup> to be correlated with the carbonyl stretching of the  $\beta$ - and  $\alpha$ -crystalline form, respectively. However, the relative intensity of the two peaks depends on the fiber size and the position within the fiber. For example, in Figure 1c, the three spectra collected on the fiber edge, E1, E2, and E3, have a relatively higher 1740 cm<sup>-1</sup> peak while the three spectra collected in the fiber center, C1, C2, and C3, have a relatively higher 1728 cm<sup>-1</sup> peak. Similar observations were made in Figure 1c'. For each fiber, the spectra collected at different spots on the edge or in the center share the same spectral shape but differ in absolute intensity. This might be due to the rough surface of the fiber affecting the contact of the AFM tip on the fiber surface from spot to spot.

Spectra C1, E1 (spectra in red) and C1', E1' (spectra in black) were plotted in the same figure as shown in Figure 3. For comparative purposes, the intensities of the highest peaks of all spectra were normalized to 1.0. By comparing C1 and C1', we observed that both spectra have characteristic peaks at 1728 and 1740 cm<sup>-1</sup>, although the 1740 cm<sup>-1</sup> peak in C1 has a much higher intensity than that in C1', indicating that through the core area the 263 nm diameter fiber has more  $\beta$  crystalline content than the 390 nm diameter fiber. By comparing the color paired two groups of curves, i.e., C1, E1 (solid spectra) and C1', E1' (dashed spectra), we noticed that E1 and E1' always tend to have a much higher 1740 cm<sup>-1</sup> peak compared

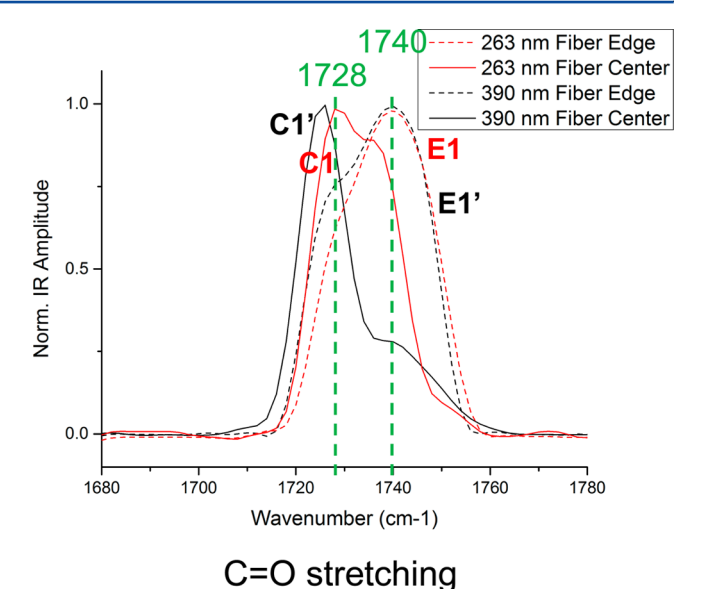


**Figure 3.** Comparison of AFM-IR spectra collected from different positions on the two individual electrospun PHBHx nanofibers.

to C1 and C1'. This observation indicates that the morphology of the polymer chains indeed shows heterogeneity throughout a single fiber, and the shell contains more  $\beta$ -form crystals than the core. Interestingly, when comparing E1 and E1', there is not much difference between the two spectra in terms of band shape, which suggests that the crystal structure or the chain morphology in the shell is independent of fiber size.

Additional support for the conclusion that the rotary disk aligned, electrospun PHBHx nanofibers have a core-shell structure comes from an investigation of the cross sections of the fibers. Figures 4a and 4a' show the AFM height image of the cross sections of two rotary disk aligned fibers from the same batch with diameters of 260 and 312 nm, respectively. Again, IR images were captured at the two characteristic frequencies of 1740 and 1728 cm<sup>-1</sup>. In order to eliminate the influence of sample thickness variation and thermal drift, the ratio of the two mappings, i.e.  $I_{1740}/I_{1728}$ , was taken as shown in Figures 4b and 4b'. The color bar indicates the increase of the relative intensity of the IR absorption from purple to red. Since the 2 Ton epoxy has negligible absorption of the IR laser at 1740 and 1728 cm<sup>-1</sup>, the IR mapping ratio in the epoxy area should equal 1, which is represented by the green/yellow color in Figures 4b and 4b'. As shown, for each of the two fiber cross sections, a clear red ring was observed at the circumference of the fiber cross section, making a clear differentiation of the fiber cross section and the epoxy. This indicates that in the ring area the ratio of  $I_{1740}/I_{1728}$  is larger than 1, or the IR absorption at 1740 cm<sup>-1</sup> is higher than that at 1728 cm<sup>-1</sup>. This observation confirms the existence of a thin shell, which contains more  $\beta$ form crystals, in the rotary disk aligned electrospun PHBHx nanofibers. Furthermore, for both of the cross sections, the thickness of the ring is consistently found to be approximately 10 nm, which is comparable with the width of the red lines along the fiber edges in Figures 1b and 1b'. This strongly suggests that the thickness of the shell in the fibers is about 10 nm, regardless of the fiber diameter. In addition, it is also observed that in Figure 4b the color in the core area of the fiber cross section is yellow, which shifts toward the red direction compared to the green color in the epoxy area. This indicates a slightly higher content of  $\beta$ -form than the  $\alpha$ -form in the core.

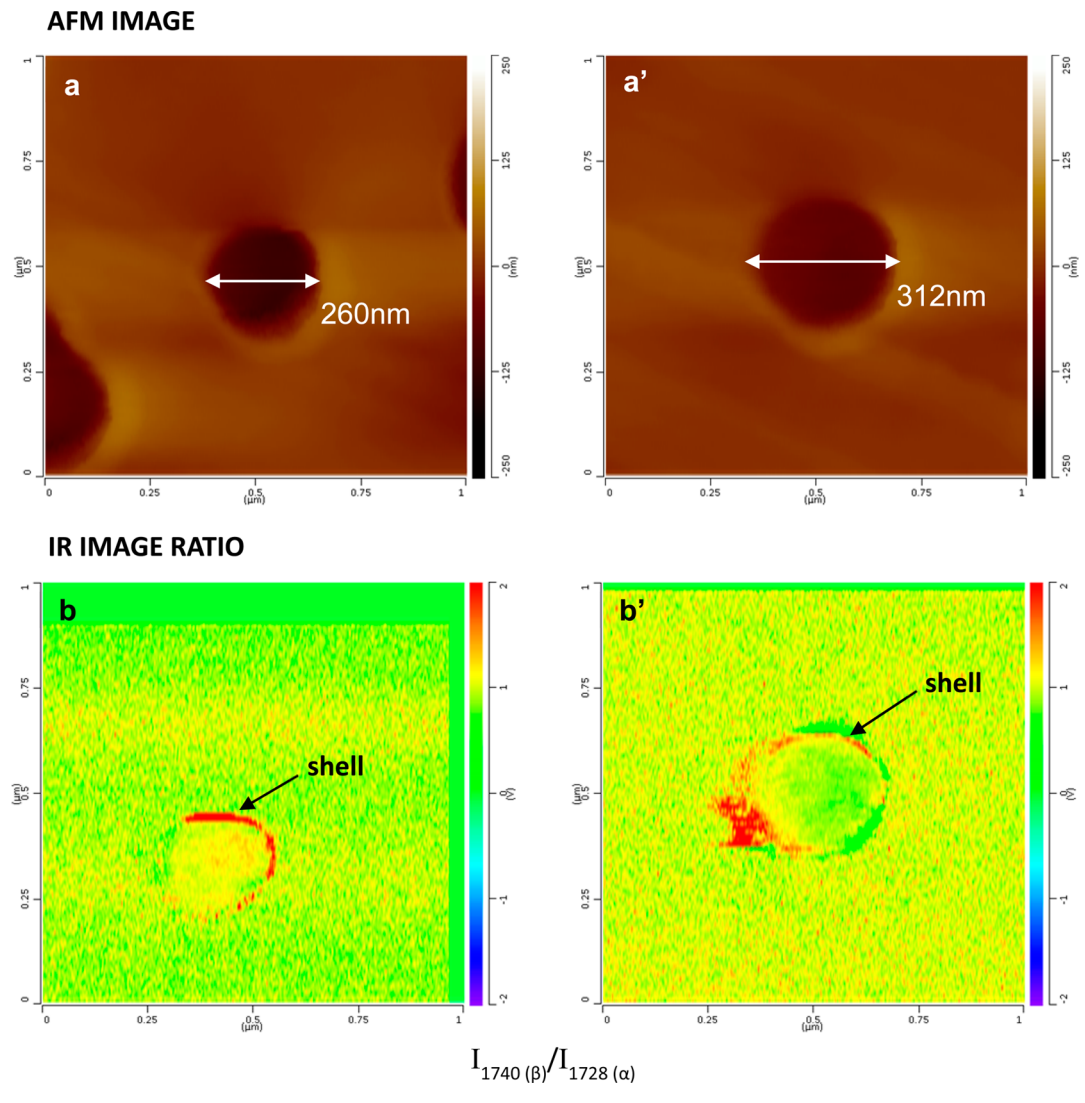


Figure 4. AFM height image (a, a') and IR peak image ratios (b, b') of the cross sections of two individual electrospun PHBHx nanofibers.

Conversely, in Figure 4b' the color in the core area is green, which shifts toward the purple direction compared to the yellow color in the epoxy area, indicating a lower content of  $\beta$ -form than the  $\alpha$ -form. This observation is consistent with the observation in Figure 3 where the 1740 cm<sup>-1</sup> peak in spectrum C1 is higher than that in C1'. However, the ring is not intact around the circumference of the fiber cross section (Figure 4b), and there is some extra red area beyond the ring (Figure 4b'). This most likely is due to the smearing of the polymer during the microtoming process, which causes a random burst or contraction of the polymer if the diamond knife is dull or the cutting speed is slow.

On the basis of the experimental observations, we propose a possible mechanism for the generation of polymorphic heterogeneous core—shell structure in the electrospun PHBHx nanofibers collected with a rotary disk, which is illustrated in Figure 5. The dissolved polymer chains in their random coil state are highly stretched during electrospinning resulting in chain extension and orientation along the stretching direction. As a result, the amorphous fibers arriving at the rotary disk consist of oriented polymer chains along the fiber axis that are plasticized by remaining solvent. During collection, the amorphous fibers are further stretched by the additional

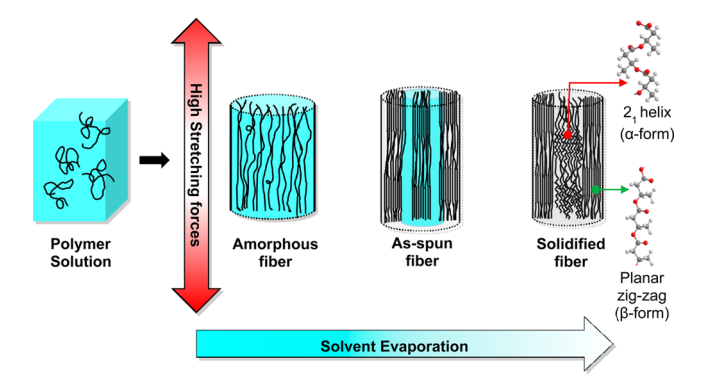


Figure 5. Possible generation mechanism for the formation of the core—shell structure of the electrospun PHBHx nanofibers collected with a rotary disk. The wavy curves in the core of the final solidified fiber are indicative of the  $2_1$  helical backbones of the chains in the α-crystalline form; the straight lines in the as spun fiber and the shell of the final solidified fiber illustrate the planar zigzag backbones of the chains in the β-crystalline form; the random curves illustrate the free chains in the amorphous region. The blue color in this figure represents solvent. The thickness of the shell is exaggerated for display purposes.

elongation forces provided by the high-speed rotating wheel. At the highest elongation, most of the polymer chains in the amorphous fiber are fully extended and adopt a planar zigzag conformation as depicted in the as spun fiber in Figure 5. Because of the extremely rapid solvent evaporation rate at the surface of the fiber, the planar zigzag chains near the surface will be kinetically frozen and crystallize into the metastable  $\beta$ -form. Thus, a thin layer of skin or shell is formed. Later, the solidified shell would act as a semipermeable barrier, limiting evaporation of the residual solvent in the core. As a result, a portion of the chains, especially in the core, would relax and convert to the more stable helical conformation ( $\alpha$ -form). Therefore, the final solidified fibers would have a core—shell structure where crystal structures are different in the core and in the shell.

This core-shell model of the spatial distribution of the  $\alpha$ and  $\beta$ -form polymorphs could largely facilitate the understanding of the structure/processing/properties relationships for PHBHx nanofibers. The  $\alpha$ - and  $\beta$ -form crystal structures, with the same chemical composition but different molecular packing, have been reported to have distinctive properties, including mechanical properties, biodegradability, and piezoelectricity. For instance, it has been widely recognized<sup>21-</sup> the  $\beta$ -form P(3HB) has much higher strength and modulus than its  $\alpha$ -form counterpart. Study of the enzymatic degradation of P(3HB)<sup>27,28</sup> revealed that the degradation rate of the  $\beta$ -phase with an *all-trans* conformation is higher than that of the  $\alpha$ -phase with a helical conformation. More interestingly, recent experimental results have shown that a piezoelectric response of the PHBHx nanofibers is most likely correlated with the introduction of the  $\beta$ -form crystal structure. Therefore, the final properties of the PHBHx nanofibers can be largely influenced by the composition of the  $\alpha$ - and  $\beta$ -phases, which is highly dependent on the electrospinning conditions. According to the core-shell model, if the application of the PHBHx nanofibers requires properties dominated by the  $\beta$ -crystalline structure, we could increase the absolute content of the  $\beta$ -form by increasing the overall stretching forces during electrospinning or expediting solvent evaporation to make it faster than solvent diffusion in the radial direction. In addition, we could increase the relative content of the  $\beta$ -form by reducing the fiber diameter in order to increase the relative volume fraction of the  $\beta$ -phase-rich shell.

# CONCLUSIONS

For the first time, the spatial distribution of crystalline polymorphs in single electrospun nanofibers was studied with the aid of the AFM-IR technique. Electrospun PHBHx nanofibers containing two crystalline polymorphs, the thermodynamically stable  $\alpha$ -form consisting of chains with a  $2_1$  helical conformation and the metastable  $\beta$ -form consisting of chains with a planar zigzag conformation, were investigated. The coexistence of the  $\alpha$ - and  $\beta$ -form polymorphs at the single fiber scale was demonstrated by the AFM-IR spectra and imaging of single PHBHx nanofibers and was reaffirmed by the SAED results. In addition, the molecular orientation level and the concentration of the  $\beta$ -form were confirmed to be highly dependent on the fiber diameter. More importantly, the AFM-IR spectra and imaging revealed that the two crystalline polymorphs were spatially distributed as a heterogeneous, core-shell structure consisting of a  $\alpha$ -form-rich core and  $\beta$ form-rich shell. The thickness of the shell remained constant though the fiber size varied, indicating that the formation of the shell is predominantly controlled by the competition between

the evaporation and diffusion of the solvent. Based on the above experimental observations, a possible generation mechanism of the core-shell structure was proposed. During fiber solidification, the planar zigzag chains, originating from the highly oriented free chains in the fiber, were kinetically frozen near the fiber surface and formed the  $\beta$ -form-rich shell due to the extremely high solvent evaporation rate at the surface. The zigzag chains in the core area of the fiber relax and convert to more stable helical chains forming the  $\alpha$ -form-rich core. This is allowed by the existence of residual solvent, evaporation of which was hindered by the more densely packed shell. This study showed that the AFM-IR technique is indeed an effective and efficient tool for the nanoscale investigation of single electrospun fibers providing both topographic and structural information at a spatial resolution well below the diffraction limit in the infrared. This study could be considered as a template for the nanoscale structural investigation of a variety of polymorphic materials when electrospinning facilitates the formation of metastable crystalline phases, such as nylon-6 and poly(vinylidene fluoride) (PVDF). The investigation of the polymorphic distribution in nanofibers as a function of processing/collection conditions provides us with a deeper understanding of the molecular chain behavior under extremely high shearing/stretching forces plus ultrafast solvent evaporation rate during electrospinning. This level of fundamental understanding of structure/property/process relationships is a critical first step toward the rational design and fabrication of polymeric nanofibers with specific properties which are end-use driven.

#### AUTHOR INFORMATION

# **Corresponding Author**

\*E-mail rabolt@udel.edu (I.F.R.).

ORCID (

David C. Martin: 0000-0003-1195-3838 John F. Rabolt: 0000-0003-4132-4266

Note

The authors declare no competing financial interest.

### ACKNOWLEDGMENTS

The authors acknowledge the support from Delaware NSF EPSCoR Grant # 1301765 and the NSF DMR Polymers Program Grant DMR-1407255. D.C.M. thanks the NSF through Polymers Program Grant DMR-1103027.

#### REFERENCES

- (1) Wendorff, J. H.; Agarwal, S.; Greiner, A. Nature of the Electrospinning Process Experimental Observations and Theoretical Analysis. In *Electrospinning*; Wiley-VCH Verlag GmbH & Co. KGaA: 2012; pp 29–68.
- (2) Rodriguez, I. A.; Mccool, J. M.; Bowlin, G. L. Functional Nanofibers for Tissue Engineering Applications. *Functional Nanofibers and their Applications* **2012**, 171–196.
- (3) Wei, Q.; Wei, A. Functional Nanofibers for Drug Delivery Applications. Functional Nanofibers and their Applications 2012, 153–170.
- (4) Wang, X. F.; Ding, B.; Yu, J. Y. Functional Nanofibers in Sensor Applications. Functional Nanofibers and their Applications 2012, 209–235.
- (5) Lopes Da Silva, J. A. Functional Nanofibers in Food Processing. Functional Nanofibers and their Applications 2012, 262–304.

(6) Ma, H.; Chu, B.; Hsiao, B. S. Functional Nanofibers for Water Purification. Functional Nanofibers and their Applications 2012, 331–370

- (7) Lee, K. H.; Kim, K. W.; Pesapane, A.; Kim, H. Y.; Rabolt, J. F. Polarized FT-IR Study of Macroscopically Oriented Electrospun Nylon-6 Nanofibers. *Macromolecules* **2008**, *41* (4), 1494–1498.
- (8) Liu, Y.; Cui, L.; Guan, F.; Gao, Y.; Hedin, N. E.; Zhu, L.; Fong, H. Crystalline Morphology and Polymorphic Phase Transitions in Electrospun Nylon-6 Nanofibers. *Macromolecules* **2007**, 40 (17), 6283–6290.
- (9) Stephens, J. S.; Chase, D. B.; Rabolt, J. F. Effect of the Electrospinning Process on Polymer Crystallization Chain Conformation in Nylon-6 and Nylon-12. *Macromolecules* **2004**, *37* (3), 877–881.
- (10) Yee, W. A.; Nguyen, A. C.; Lee, P. S.; Kotaki, M.; Liu, Y.; Tan, B. T.; Mhaisalkar, S.; Lu, X. Stress-Induced Structural Changes in Electrospun Polyvinylidene Difluoride Nanofibers Collected Using a Modified Rotating Disk. *Polymer* **2008**, *49* (19), 4196–4203.
- (11) Zheng, J.; He, A.; Li, J.; Han, C. C. Polymorphism Control of Poly(vinylidene Fluoride) through Electrospinning. *Macromol. Rapid Commun.* **2007**, 28 (22), 2159–2162.
- (12) Kongkhlang, T.; Kotaki, M.; Kousaka, Y.; Umemura, T.; Nakaya, D.; Chirachanchai, S. Electrospun Polyoxymethylene: Spinning Conditions and Its Consequent Nanoporous Nanofiber. *Macromolecules* **2008**, *41* (13), 4746–4752.
- (13) Yee, W. A.; Kotaki, M.; Liu, Y.; Lu, X. Morphology, Polymorphism Behavior and Molecular Orientation of Electrospun Poly(vinylidene Fluoride) Fibers. *Polymer* **2007**, *48* (2), 512–521.
- (14) Gong, L.; Chase, D. B.; Noda, I.; Liu, J.; Martin, D. C.; Ni, C.; Rabolt, J. F. Discovery of  $\beta$ -Form Crystal Structure in Electrospun Poly[(R)-3-Hydroxybutyrate-Co-(R)-3-Hydroxyhexanoate] (PHBHx) Nanofibers: From Fiber Mats to Single Fibers. *Macromolecules* **2015**, 48 (17), 6197–6205.
- (15) Marcott, C.; Lo, M.; Kjoller, K.; Prater, C.; Noda, I. Spatial Differentiation of Sub-Micrometer Domains in a Poly-(hydroxyalkanoate) Copolymer Using Instrumentation That Combines Atomic Force Microscopy (AFM) and Infrared (IR) Spectroscopy. *Appl. Spectrosc.* 2011, 65 (10), 1145–1150.
- (16) Nasse, M. J.; Walsh, M. J.; Mattson, E. C.; Reininger, R.; Kajdacsy-Balla, A.; Macias, V.; Bhargava, R.; Hirschmugl, C. J.; Hirschmug, C. J. High-Resolution Fourier-Transform Infrared Chemical Imaging with Multiple Synchrotron Beams. *Nat. Methods* **2011**, *8* (5), 413–416.
- (17) Walsh, M. J.; Kajdacsy-Balla, A.; Holton, S. E.; Bhargava, R. Attenuated Total Reflectance Fourier-Transform Infrared Spectroscopic Imaging for Breast Histopathology. *Vib. Spectrosc.* **2012**, *60* (217), 23–28.
- (18) Dazzi, A.; Glotin, F.; Carminati, R. Theory of Infrared Nanospectroscopy by Photothermal Induced Resonance. *J. Appl. Phys.* **2010**, *107* (12), 124519.
- (19) Dazzi, A.; Prazeres, R.; Glotin, F.; Ortega, J. M.; Al-Sawaftah, M.; de Frutos, M. Chemical Mapping of the Distribution of Viruses into Infected Bacteria with a Photothermal Method. *Ultramicroscopy* **2008**, *108* (7), *6*35–*6*41.
- (20) Lahiri, B.; Holland, G.; Centrone, A. Chemical Imaging beyond the Diffraction Limit: Experimental Validation of the PTIR Technique. *Small* **2013**, 9 (3), 439–445.
- (21) Aoyagi, Y.; Doi, Y.; Iwata, T. Mechanical Properties and Highly Ordered Structure of Ultra-High-Molecular-Weight poly[(R)-3-Hydroxybutyrate] Films: Effects of Annealing and Two-Step Drawing. *Polym. Degrad. Stab.* **2003**, *79* (2), 209–216.
- (22) Iwata, T.; Tsunoda, K.; Aoyagi, Y.; Kusaka, S.; Yonezawa, N.; Doi, Y. Mechanical Properties of Uniaxially Cold-Drawn Films of poly([R]-3-Hydroxybutyrate). *Polym. Degrad. Stab.* **2003**, *79* (2), 217–224.
- (23) Iwata, T.; Aoyagi, Y.; Fujita, M.; Yamane, H.; Doi, Y.; Suzuki, Y.; Takeuchi, A.; Uesugi, K. Processing of a Strong Biodegradable Poly[(R)-3-Hydroxybutyrate] Fiber and a New Fiber Structure Revealed by Micro-Beam X-Ray Diffraction with Synchrotron Radiation. *Macromol. Rapid Commun.* 2004, 25 (11), 1100–1104.

(24) Furuhashi, Y.; Imamura, Y.; Jikihara, Y.; Yamane, H. Higher Order Structures and Mechanical Properties of Bacterial Homo poly(3-Hydroxybutyrate) Fibers Prepared by Cold-Drawing and Annealing Processes. *Polymer* **2004**, *45* (16), 5703–5712.

- (25) Antipov, E. M.; Dubinsky, V. A.; Rebrov, A. V.; Nekrasov, Y. P.; Gordeev, S. A.; Ungar, G. Strain-Induced Mesophase and Hard-Elastic Behaviour of Biodegradable Polyhydroxyalkanoates Fibers. *Polymer* **2006**, *47* (15), 5678–5690.
- (26) Tanaka, T.; Fujita, M.; Takeuchi, A.; Suzuki, Y.; Uesugi, K.; Ito, K.; Fujisawa, T.; Doi, Y.; Iwata, T. Formation of Highly Ordered Structure in Poly[(R)-3-Hydroxybutyrate- c O -(R)-3-Hydroxyvalerate] High-Strength Fibers. *Macromolecules* **2006**, *39* (8), 2940–2946.
- (27) Iwata, T.; Aoyagi, Y.; Tanaka, T.; Fujita, M.; Takeuchi, A.; Suzuki, Y.; Uesugi, K. Microbeam X-Ray Diffraction and Enzymatic Degradation of Poly[(R)-3-Hydroxybutyrate] Fibers with Two Kinds of Molecular Conformations. *Macromolecules* **2006**, 39 (17), 5789–5795
- (28) Ishii, D.; Lee, W.-K.; Kasuya, K.-I.; Iwata, T. Fine Structure and Enzymatic Degradation of poly[(R)-3-Hydroxybutyrate] and Stereocomplexed Poly(lactide) Nanofiber. *J. Biotechnol.* **2007**, *132* (3), 318–324.